scientific reports

Check for updates

OPEN

Relevant methane emission to the atmosphere from a geological gas manifestation

Adriano Mazzini[1]✉, Alessandra Sciarra[2], Giuseppe Etiope[2,3], Pankaj Sadavarte[4,5], Sander Houweling[4,6], Sudhanshu Pandey[4] & Alwi Husein[7]

Quantifying natural geological sources of methane (CH_4) allows to improve the assessment of anthropogenic emissions to the atmosphere from fossil fuel industries. The global CH_4 flux of geological gas is, however, an object of debate. Recent fossil (^{14}C-free) CH_4 measurements in preindustrial-era ice cores suggest very low global geological emissions (~ 1.6 Tg year^{-1}), implying a larger fossil fuel industry source. This is however in contrast with previously published bottom-up and top-down geo-emission estimates (~ 45 Tg year^{-1}) and even regional-scale emissions of ~ 1–2 Tg year^{-1}. Here we report on significant geological CH_4 emissions from the Lusi hydrothermal system (Indonesia), measured by ground-based and satellite (TROPOMI) techniques. Both techniques indicate a total CH_4 output of ~ 0.1 Tg year^{-1}, equivalent to the minimum value of global geo-emission derived by ice core $^{14}CH_4$ estimates. Our results are consistent with the order of magnitude of the emission factors of large seeps used in global bottom-up estimates, and endorse a substantial contribution from natural Earth's CH_4 degassing. The preindustrial ice core assessments of geological CH_4 release may be underestimated and require further study. Satellite measurements can help to test geological CH_4 emission factors and explain the gap between the contrasting estimates.

Methane (CH_4) is a greenhouse gas 28 times more powerful than carbon dioxide (CO_2) on a 100 year time horizon[1]. It is released to the atmosphere by both natural and anthropogenic sources, with a global emission of ~ 560 teragrams per year (Tg year^{-1})[2,3]. About 30% of this methane is fossil[4], characterized by the absence of radiocarbon (^{14}C) that is present in modern biological gas. Fossil CH_4 is mostly released by fugitive emissions during oil and gas extraction and distribution, and coal mining (about 100–145 Tg year^{-1}[3,5]). In addition, CH_4 is also naturally emitted through the Earth's degassing via surface gas manifestations (seeps, mud volcanoes, diffuse microseepage) in petroleum-bearing sedimentary basins and geothermal areas (e.g.[6]). Understanding the strength of this geological source provides better constraints on the anthropogenic fossil fuel fraction[5,7]. Bottom-up emission estimates (based on inventories and measurements of emission factors) and top-down estimates (atmospheric and ice core data and inverse modelling) converge to a global geo-CH_4 output of around 45 Tg year^{-1} (from 27 to 70 Tg year^{-1}) (e.g.[8]). In contrast, recent estimates based on preindustrial-era ice core $^{14}CH_4$ measurements suggest values one to two orders of magnitude lower (from 0.1 to 5.4 Tg year^{-1}, with a median value of 1.6 Tg year^{-1})[7], which would greatly increase the estimate of the anthropogenic fossil fuel fraction. Hmiel et al.[7] based their study on the measurements of the amount of fossil CH_4 present in the air trapped in preindustrial ice cores, and thus before the influence of hydrocarbon exploration and production. The CH_4 contribution from the fossil fuel industry was inferred by assuming that the measured ice-core CH_4 represents the natural geological emissions, and also expecting that this natural degassing remained relatively constant over the last few centuries.

In short, there is a large discrepancy between the geological CH_4 source estimates by Hmiel et al.[7] and those previously proposed by several scholars for specific types of geological sources, e.g. mud volcanoes[6,9,10];

[1]Centre for Earth Evolution and Dynamics (CEED), University of Oslo, Oslo, Norway. [2]Istituto Nazionale di Geofisica e Vulcanologia, via di Vigna Murata 605, 00143 Rome, Italy. [3]Faculty of Environmental Science and Engineering, Babes Bolyai University, Cluj-Napoca, Romania. [4]SRON Netherlands Institute for Space Research, Earth Science Group (ESG), Utrecht, The Netherlands. [5]Department of Climate, Air and Sustainability, TNO, Utrecht, The Netherlands. [6]Department of Earth Sciences, Vrije Universiteit, Amsterdam, The Netherlands. [7]Pusat Pengendalian Lumpur Sidoarjo (PPLS), Suarabaya, Indonesia. ✉email: adriano.mazzini@geo.uio.no

microseepage[11,12]; and submarine seeps[8,13,14]. This disparity appears even more striking when considering local and regional geo-CH_4 emission estimates. For example seeps in Alaska have an estimated CH_4 release of 0.7–1.4 Tg $year^{-1}$[15], while submarine seeps in the East Siberian Arctic Shelf have a total CH_4 output to the atmosphere of 3 Tg $year^{-1}$[16]. The Hmiel et al.[7] estimate is inconsistent with field flux measurements, since it would imply seepage emission factors one to two orders of magnitude lower than those assessed so far (for example, about 3000–6000 tonnes km^{-2} $year^{-1}$ for mud volcanoes[6]).

Here, we report CH_4 emissions from a single, large gas manifestation whose flux is already within the lower range of the global estimate derived by ice core $^{14}CH_4$ measurements. For the first time, satellite (TROPOMI) observations are used to test and support ground-based flux measurements. The degassing site is known as Lusi ('LUmpur' -meaning mud in Indonesian, and 'SIdoarjo' -the district name), located in the northeast Java Island, Indonesia[17]. Lusi is a hybrid Sediment-Hosted Geothermal System (SHGS)[18,19] triggered after the 27th May 2006 Java earthquake[20]. Numerous mud bursting vents appeared on the 29th of May 2006, almost two days after a 6.3 M earthquake struck the island. These eruption sites developed over a distance of > 1 km along a system of fractures that follows the orientation of the Watukosek fault system[20]. This is a NE-SW regional tectonic discontinuity running from the Arjuno-Welirang (AW) volcanic arc towards the NE of Java, intersecting Lusi and several mud volcanoes (e.g.[21–23]). Within weeks after the inception, the active eruption sites expanded in size, with the largest one developing a 100 m wide vent releasing boiling water, mud, rock clasts, oil and gas. Up to 180,000 m^3 day^{-1} of mud were expelled, resulting in submerged villages and displacement of more than 60,000 people[20,24]. Two major vents currently erupt in the crater zone, alternating between periods of regular activity and powerful geysering events, making Lusi a clastic-dominated geysering-like system[25]. These two Lusi vents are isolated inside a ~ 650 m diameter circular pond of fluidized mud, framed by a vast area of dry mud breccia hosting thousands of bubbling seeps. The region covered with mud breccia spans over ~ 7 km^2 and is confined by a tall embankment built to prevent flooding expansion (Fig. 1A).

Central vents at Lusi primarily discharge aqueous vapour (~ 98 vol.%) belonging to the hydrothermal component of the system. In addition, CH_4 and CO_2, are released at variable concentrations both from the boiling vents, satellite peripheral seeps, and fractured ground[18,23,26]. Converging geophysical, geochemical, petrography, and modelling data indicate that magmatic/hydrothermal CO_2-rich fluids, migrating from the neighbouring AW volcanic complex, flushed through the hydrocarbon-rich back-arc sedimentary basin triggering the formation of over-pressurised gas pools[18,27–32].

Here, we estimate the total CH_4 emissions from Lusi using both ground-based and satellite (TROPOMI) measurements (Figs. 1, 2, 3). CO_2 emission is additionally measured by ground-based techniques. Ground-based and remote sensing methods provide very similar estimates, confirming the order of magnitude of the emission factors of large seeps used in global bottom-up emission estimates[6].

Results

Gas emission structures and related fluxes. We studied and classified the Lusi degassing modes identified throughout the region inside the embankment and performed CH_4 and CO_2 flux measurements in all of them (Figs. 1, 2). We recognised that, in addition to two main *central vents* (active in what we define as the crater zone), the gas exhales abundantly from three different emission modes: (a) diffuse invisible seepage (*miniseepage*) occurring throughout the area covered by mud, (b) degassing through a network of *fractures,* parallel and antithetic to the Watukosek fault system, and (c) thousands of *satellite seeps* scattered around the crater zone inside the embankment area (see details in "Supplementary Material", Fig. 2). For each of these degassing modes we applied specific ground-based flux measurement approaches, including the closed-chamber method (655 flux measurements), crater plume monitoring and volume measurements (205 measurements), and up-scaling techniques following widely used methods in geological gas emission studies ("Methods" and "Supplementary Material").

Table 1 and Fig. 1B show the CH_4 and CO_2 fluxes released to the atmosphere from the four Lusi degassing modes (i.e. crater zone, miniseepage, fractured zones and satellite seeps). Details of flux calculations are provided in the "Supplementary Material", Figs. S1, S2, S3 and S4. The main vent, whose gas composition is characterized by an average CO_2/CH_4 ratio ~ 3[18,26], releases in total ~ 42 (from 26 to 61) ktonnes CH_4 $year^{-1}$, and ~ 340 (from 213 to 496) ktonnes CO_2 $year^{-1}$. The gas flux from the second vent was not measured, but long-term observations and video records show that its activity is similar to that of the main vent with a focussed plume of ~ 35 m in diameter. Using the same approach applied for the main vent, we calculate a mean emission of ~ 22 ktonnes CH_4 $year^{-1}$, and ~ 176 ktonnes CO_2 $year^{-1}$. Details for crater zone emission estimates are provided in the "Supplementary Material".

The surrounding area, including fractures, satellite seeps and diffuse degassing (miniseepage) over ~ 7 km^2, releases ~ 38 ktonnes CH_4 $year^{-1}$, and ~ 24 ktonnes CO_2 $year^{-1}$. Ground-based flux measurements suggest, therefore, a total CH_4 emission of around 0.1 Tg $year^{-1}$ (78.3–131.5 ktonnes $year^{-1}$) (Fig. 1B, Table 1).

The amount of CH_4 released from the crater zone and that from the surrounding degassing are of the same order of magnitude. CO_2 instead is mostly released from the vents, representing the core of the hydrothermal manifestation as indicated by hot fluids and abundant water vapour. It has been suggested that the CO_2-dominated gas released from the vents results from the rapid de-pressurization of the fast-rising fluids combined with the exsolution of the dissolved pore water gas ongoing at high temperatures (i.e. > 100 °C) at near surface conditions[18,20]. The gas from the satellite seeps is instead CH_4-enriched. The degassing in the surrounding zone is likely related to colder peripheral pathways that branch off from the main conduit in combination with release of gas stored within the thick deposits of mud breccia[18]. These deposits range in thickness from hundreds to tens of metres with increasing distance from the central area[33,34].

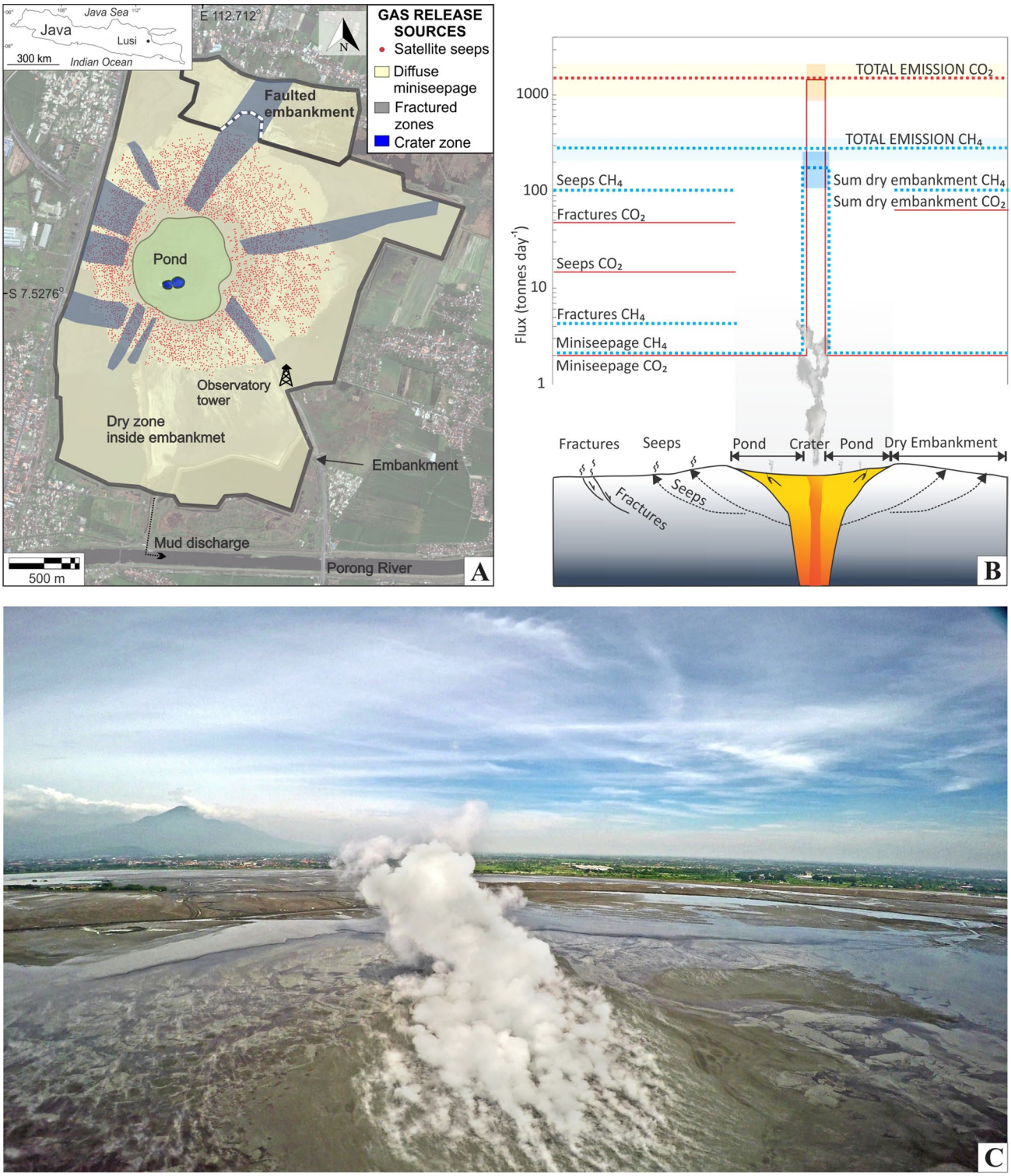

Figure 1. Gas emissions at Lusi site. (**A**) High resolution Ikonos satellite image of Lusi area in August 2014; Additional details, exported from basemap obtained from Esri ArcGIS ArcMap 10.2.1 and overlaid using Corel Draw X7, indicate the main features and the gas release sources identified in the region. Inset map of Java Island with indicated Lusi location. (**B**) Detailed outputs of gas emissions from the different sources around the eruption site. (**C**) Drone view of the plume during its regular geysering activity. The second vent is behind the main one and the Arjuno-Welirang volcanic complex in the background. The inaccessible 650 m in diameter pond surrounding the crater zone is filled by hot mud and laterally extensive oil slicks.

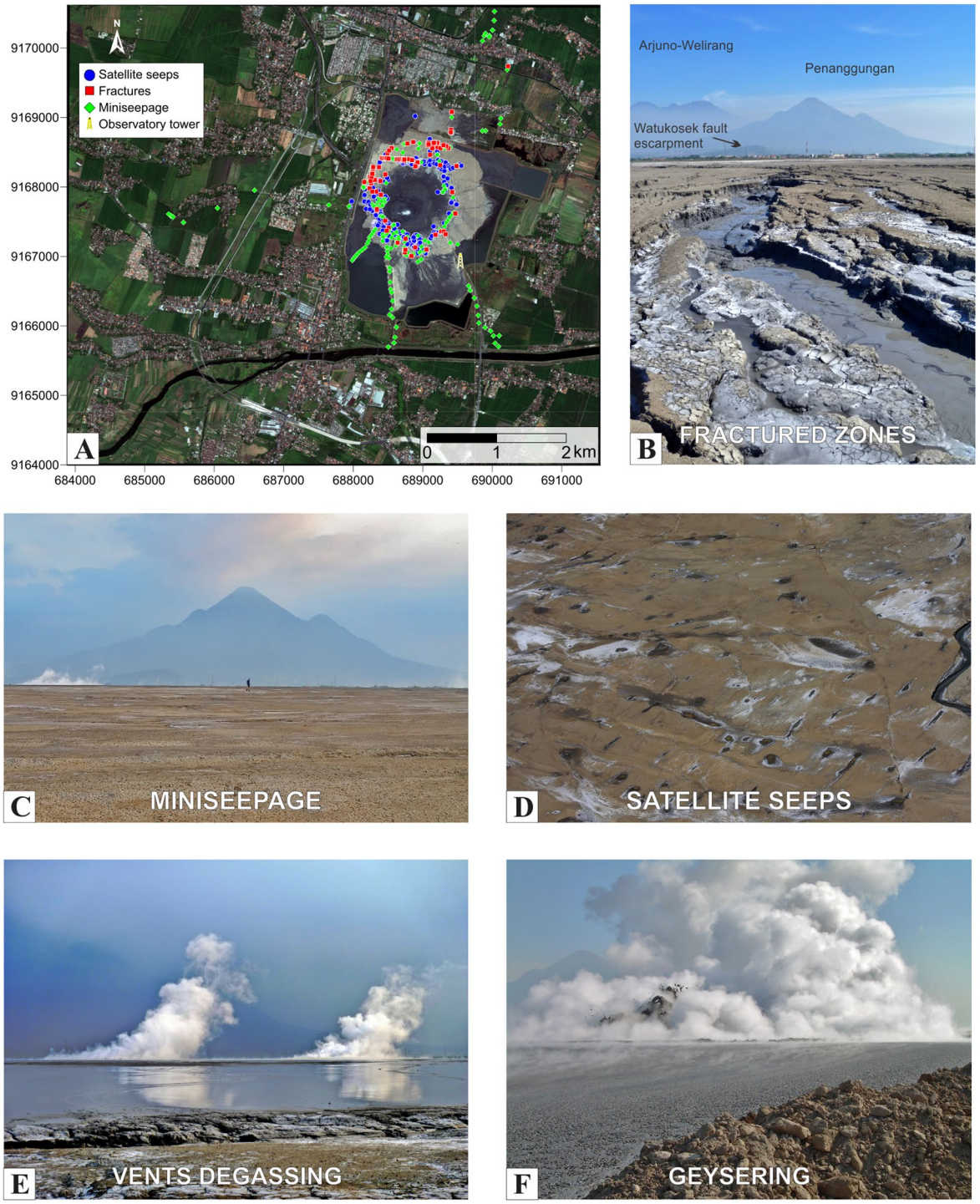

Figure 2. Measurements and identified gas release sources at Lusi. (**A**) High resolution Ikonos satellite image of Lusi area in August 2014 with additional overlaid basemap constructed using Esri ArcGIS ArcMap 10.2.1. Symbols indicate the positions, and the equivalent degassing modes, of the flow measurements done with accumulation chamber. (**B**–**E**) The four main degassing modes identified in this study: (**B**) fractured zone extending in NE–SW direction towards the volcanic complex in the background; (**C**) field view of the vast region where miniseepage occurs in undisturbed surface; (**D**) aerial view of dozens of satellite seeps (for scale the stream on the right side is ~ 1 m wide); (**E**) the two active vents during regular activity, view from the edge of the not accessible pond. (**F**) Example of geysering activity.

We stress that the gas emission estimates are conservative. They do not include the continuous degassing in the 650 m diameter circular pond framing the crater zone. In this inaccessible area, we assigned a low averaged

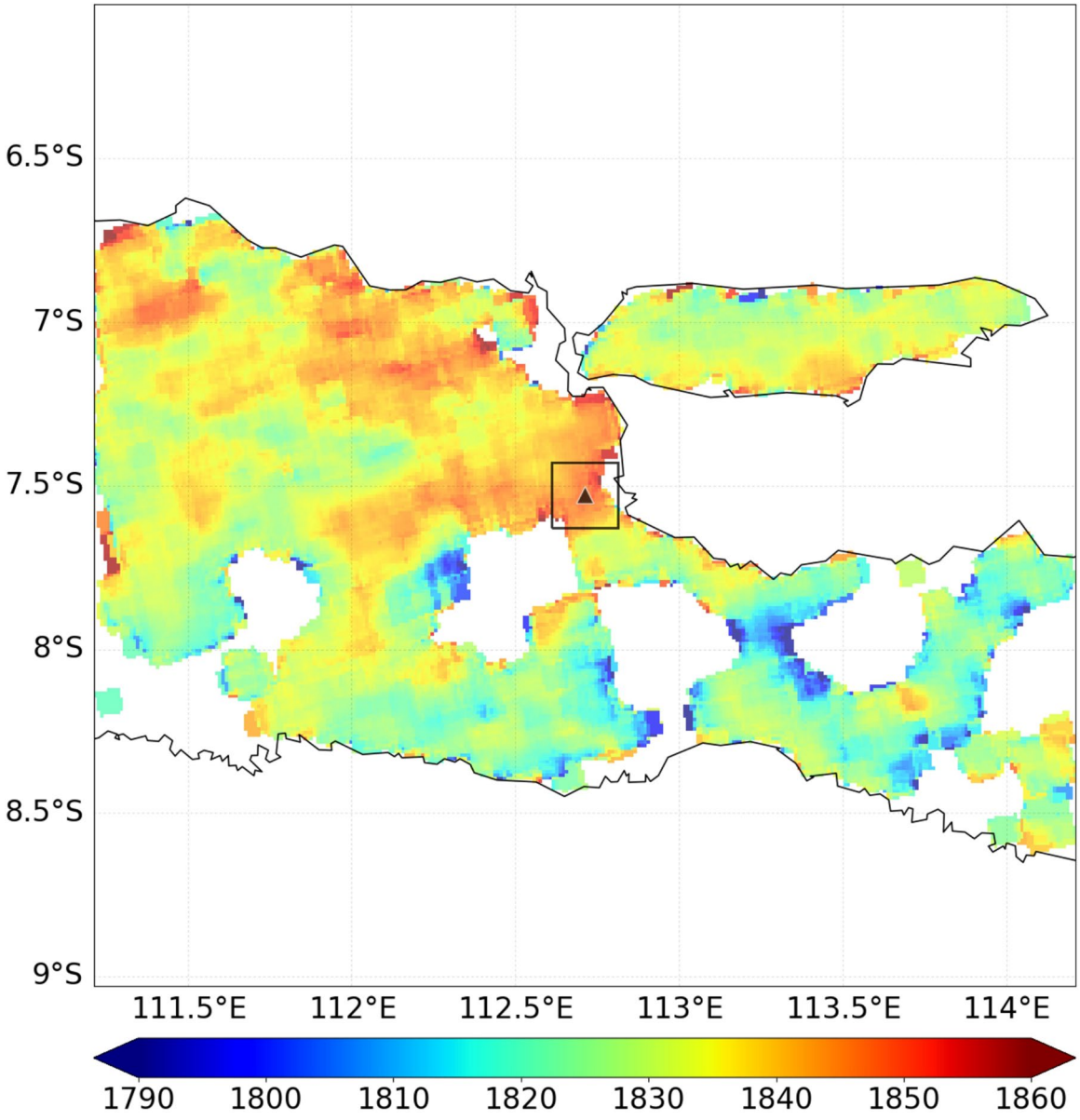

Figure 3. An oversampled (0.01° × 0.01°) map of TROPOMI data averaged over the study domain from May 2018 till July 2019. The location of Lusi is indicated by a triangle and the square denotes the source box. Units in ppb. Map generated using Python 2.7.13 version.

soil miniseepage value, however aerial images show intense and ongoing diffuse gas bubbling activity. In addition, the crater zone emission was calculated during Lusi steady state degassing (i.e. regular activity). Importantly, our budget does not include the powerful geysering activity that characterizes Lusi for about fifty percent of the time[25]. Ultimately, elevated air content estimates within the plume volume (i.e. 75%) were considered in our calculations, although video records often showed an apparently more homogenously dense gas plume.

Figure S4C shows the monitoring of Lusi mud flow rate since the inception in May 2006. Between 2014 and 2016 (i.e. survey time described herein) Lusi had the lowest recorded flow rate. Previous studies revealed that a direct correlation exists between the increase in flow rate and the gas released from the plume[25,35,36]; therefore our conservative degassing estimates can safely be applied throughout Lusi's activity. Daily observations, videos, and monitoring show that during the first years Lusi had long-lasting geysering phases and higher mud flow rates (i.e. up to 180,000 m^3 day^{-1}), and developed a system of vigorous satellite seeps extending for kilometres around the main crater zone. Therefore, much greater degassing is expected to have occurred between 2006 and 2011, and from the end of 2015 until the end of 2018. Interpolating our flow rate measurements (Fig. S4C), we calculate that between May 2006 and January 2019 Lusi discharged a total of ~ 0.3 km^3 of mud breccia.

TROPOMI satellite measurements. We obtained an independent emission estimate from TROPOMI retrievals of total column CH_4 (XCH_4) collected over eastern Java between May 2018 and July 2019 (Fig. 3).

Seepage mode	N. data	ϕCH_4 (tonnes year^{-1})	ϕCO_2 (tonnes year^{-1})	ϕCH_4 (tonnes km^{-2} year^{-1})	ϕCO_2 (tonnes km^{-2} year^{-1})	Area (km^2)
Vent1 LOW		26,350	212,822			
Vent1 MEAN	205[a]	42,040	339,551			
Vent1 MAX		61,372	495,690			
Vent2 LOW		13,660	110,327			
Vent2 MEAN		21,794	176,023			
Vent2 MAX		31,815	256,965			
Miniseepage LOW		346	471	59	80	
Miniseepage MEAN	175	774	734	131	124	5.91
Miniseepage MAX		2047	1752	346	296	
Fractured zones LOW		15	5595	12	4176	
Fractured zones MEAN	129	1573	17,484	1174	13,047	1.34
Fractured zones MAX		7022	36,586	5240	27,303	
Satellite seeps	351	35,960	5325			
Total excluding crater zone		38,307	23,543			
Total LOW		78,316	346,692	10,802	47,820	
Total MEAN		102,141	539,117	14,088	74,361	7.25
Total MAX		131,494	776,198	18,137	107,062	
TROPOMI LOW		53,000				
TROPOMI MEAN		140,000				
TROPOMI MAX		227,000				

Table 1. CH_4 and CO_2 fluxes released to the atmosphere from the four Lusi degassing systems (two vents in the crater zone, miniseepage, fractured zones and satellite seeps) estimated by ground-based measurements. [a]Number of vent plume measurements; ϕ = estimated gas flux. The accuracy of the flux measurements completed with the portable fluximeter inside the embankment zone (miniseepage, fractures zones and satellite seeps) is ± 10%.

XCH_4 enhancements are found in the Surabaya and Sidoarjo region, including the location of Lusi, on the order of 8–9 ppb. We estimated the CH_4 emissions from Lusi of 140 ± 87 ktonnes year^{-1} using the mass balance approach (see "Methods"). Figure 1A,B highlight the presence of many smaller (fractured zone, mini seepage, satellite seeps) and larger (crater zone) methane emitting seepage modes present throughout the area considered. Similarly, Table 1 shows that the crater (situated in the center) emits around 40–93 ktonnes year^{-1} methane while satellite seeps, which are uniformly spread across the whole area accounts for a total of 36 ktonnes year^{-1}, with a smaller fraction from other seepage mode (0.5–9 ktonnes year^{-1}). Given this variety in methane fluxes, we expect to detect diffuse XCH_4 enhancements rather than distinct plumes in TROPOMI. The higher estimated emissions from TROPOMI are consistent with a higher mud flow rate measured during 2018–2019 compared to that measured during the 2014–2016 ground-based survey period. However, the relatively high TROPOMI estimates are not linearly related to the increase in mud flow rate observed for the in-situ measurements (Fig. S4C). The low mean estimate from TROPOMI can be due to overestimation of anthropogenic emissions in EDGAR (see more details in "Supplementary Material"). Also, the low wind speeds observed in the region introduces uncertainty (tabulated in Table S1 and Fig. S6A). The larger uncertainty bound of the satellite-derived emissions can accommodate a source rate > 200 ktonnes year^{-1}, which is significantly larger than the ground-based estimation. The high uncertainty in the TROPOMI-derived estimate is mainly due to sensitivity to the choice of the background and source box, as well as the difficulty to unequivocally distinguish Lusi emissions from others anthropogenic sources in the region. The anthropogenic emissions and wetland emissions are estimated to vary respectively by 12–47% and 0.04–0.4% of the total emission in source boxes varying in size between 0.2° × 0.2° and 0.7° × 0.7° in intervals of 0.1° (Fig. S5). The contribution of the surface emissions is relatively small for the smallest source box, but we cannot exclude the possibility that the local XCH_4 enhancements are influenced by surrounding emissions, particularly given the generally low wind-speeds (< 2 m s^{-1}). It is interesting to note that, aside from rare exceptions, the predominant winds throughout the monitored timeframe have easterly and south-easterly directions (Fig. S6B). No obvious methane signal can be detected to the south of Lusi despite the fact that the settlement distributions are similar to both the northern and southern side of the eruption site. This observation strengthens the fact that the TROPOMI estimates are consistent with a sizeable source from Lusi for any choice of region (Fig. S6E).

Discussion

Although Lusi is neither a pure hydrothermal system nor a magmatic volcano, its CO_2 output of ~ 0.35–0.78 Tg year^{-1} is within the range (0.006–19 Tg year^{-1}) of volcanic emissions, and comparable with the emissions of Erebus (Antarctica), White Island (New Zealand) and Augustine (USA) volcanoes (an updated list of volcanic CO_2 output are reported by[37] and Refs. therein). Large tectonic and hydrothermal/geothermal systems release CO_2 amounts similar to those measured at Lusi[37,38]. Therefore, as a geological CO_2 source, Lusi is not an exceptional case. Global volcanic CO_2 emissions (~ 600 Tg year^{-1}[37,39]) represent a very modest component of the atmospheric carbon budget, two and three orders of magnitude lower than anthropogenic and natural sources, respectively[2].

Conversely, natural geological emissions appear to be a significant fraction of the atmospheric CH_4 budget (~ 45 Tg year^{-1}[18]), roughly accounting 8% of total emissions. Recent analyses, based on preindustrial-era ice core $^{14}CH_4$ measurements, suggest instead a much lower global output, ranging from 0.1 to 5.4 Tg year^{-1}[17]. These estimates diverge also with the values reported herein, which reveal that the Lusi emissions alone already match the minimum range assessed by Hmiel et al.[7] for the entire planet. Moreover, in a global onshore seep inventory, 76 seeps were identified as "big emitters", i.e. potentially releasing methane in the order of 10^4 tonnes year^{-1}[6]. This list includes Lusi. The emission estimate in the seep inventory is based on statistically derived emission factors and seepage area calculated by image analysis (see details in[6]). An overall (vents plus diffuse seepage) emission factor of 7.1 ktonnes km^{-2} year^{-1} (statistically derived[6]) was applied to Lusi, resulting in a predicted potential release of about 50 ktonnes CH_4 year^{-1}. This is equivalent to the lower estimate by TROPOMI, or less than half the mean value estimated by either TROPOMI or ground-based techniques, which indicates an overall emission factor exceeding 14 ktonnes km^{-2} year^{-1} (~ 5.3 ktonnes km^{-2} year^{-1} excluding the crater zone). We can hypothesize that numerous of the continuously and actively degassing mud volcanoes and similar seep systems worldwide, which differently from Lusi are dominated by CH_4 and not CO_2, may have CH_4 emission factors at least of the same order of magnitude of that estimated in this work. For example, the "big emitters" inventory[6] includes 27 mud volcanoes or mud volcano clusters, mostly in Azerbaijan, with a size similar or exceeding that from Lusi. These emitters may then release CH_4 amounts of the same order of magnitude of those degassed by Lusi in the peripheral part through invisible miniseepage, fractured zones and active seeps. Such seepage potential suggests that the ice core $^{14}CH_4$ study[7] may have underestimated the natural Earth's CH_4 degassing. In any case, the discrepancy existing between the field plus satellite measurements and the ice core $^{14}CH_4$ estimates implies that the latter requires further investigations and evaluations.

The abundant methane release measured in the accessible area around Lusi's crater (i.e. excluding the crater zone) is comparable to that of major leaks related to fossil fuel industry, such as gas compressors in Turkmenistan, recently detected by the TROPOMI and GHG-Sat D satellites (about 129 ktonnes year^{-1}[40]), and it is higher than the largest reported methane point sources, coal mines and landfills, in the United States (10–100 ktonnes year^{-1}[41]).

Our results reveal that satellite-derived emission estimates are becoming a fundamental tool to validate ground-based flux measurements. Refined remote-sensing estimates may be a valid substitute for field activities that are time-consuming and often impossible to be completed in dangerous or inaccessible regions. Identification and detection of geo-methane emission points/areas, including large active seeps, vents and mud volcanoes, using satellite observations will be an essential challenge to improve global estimates of Earth's methane degassing and, indirectly, quantify the anthropogenic emission from fossil fuel industries.

Methods

This works combines the observations and measurements conducted during daily routine monitoring of the Indonesian Ministry Agencies (BPLS-PPLS) and the data collected during more than a dozen of dedicated fieldworks conducted since the beginning of the Lusi eruption in 2006. Gas flux measurements were designed and performed according to the several degassing modes (crater zone, miniseepage, fractured zones and satellite seeps, Fig. S1) described in detail in the "Supplementary Material".

CH_4 and CO_2 flux from the main vent was estimated by measuring gas plume vertical velocity (period 2015–2019), through a theodolite (Topcon AT-G2) mounted on the observatory tower located at the south-eastern part of Lusi embankment, knowing gas plume density (based on H_2O, CO_2 and CH_4 relative composition) and CH_4 and CO_2 concentration/ratio (from[18,26]). For the procedures and data elaboration, see "Supplementary Material".

Gas flux from the miniseepage, fractured zones and satellite seeps was measured by closed-chamber technique. The system used a 20 cm-diameter metallic box connected to a West System sensor package (Pontedera, Italy) including a laser CH_4 sensor (Tunable Diode Laser Adsorption detector, precision and lower detection limit of 0.1 ppmv) and an infrared CO_2 detector (LICOR–LI820, accuracy of 2% and repeatability is ± 5 ppmv). The flux is derived by measuring the concentration build-up within the box over time (e.g.[23]).

The sample site selection was mainly linked to the site logistics and the presence of dry walkable mud inside the embankment. In this area, a total of 655 CO_2 and CH_4 flux measurements were performed (during November–December 2014, June 2015 and May 2016) from the three degassing modes (Fig. 2A).

In total, 351 satellite seeps with varying amount of water content, microbial activity and extension, were measured. The flux measurements were also carried out radially from individual seeps to assess the extension of the macro-seepage area excluding miniseepage. This datum, estimated to be ~ 2 m, was important for the output estimation since it takes into account the area of the individual seeps.

In total, 129 flow measurements were carried out both along the raised edge and in the depressions present in the central part of the main fractured/faulted zones oriented NE–SW (i.e. Watukosek strike slip fault system) or through the antithetic equivalents (Siring fault system) (e.g.[21–23,33]).

In total, 175 flux measurements were carried out on diffuse invisible seepage (miniseepage) throughout the area covered by walkable dry mud, trying to obtain a distribution as homogeneous as possible of the data.

Flux data were elaborated by statistical and spatial analysis software packages (Surfer 12.0, Golden Software, Inc.; Statistica 10.0, StatSoft, Inc.; ArcGIS, ESRI, Inc.) to estimate total gas emissions ("Supplementary Material"). Miniseepage and fractured zone emissions, being areal degassing modes, were estimated by Natural Neighbour interpolation and volume method (Surfer 12.0, Golden Software, Inc.). Total emission from satellite seeps was estimated by summing individual fluxes from measured and modelled seeps ("Supplementary Material").

Recent studies[42,43] have shown independent TROPOMI estimates using the mass balance method to quantify methane emissions using XCH_4 enhancements over an area source relative to an upwind background. The study presented herein uses the mass balance method from Buchwitz et al.[44] to quantify methane emission using a background region defined based on boundary layer averaged wind speed and direction from the ECMWF ERA5 reanalysis. The contributions from anthropogenic, biomass burning and wetland emissions in the source box are accounted for using the EDGARv5.0[45], GFED4.1 s[46] and WetCHARTs version 1.0[47] emissions. A total of 50 orbits were screened for data availability in the period May 2018–July 2019 requiring > 100 valid retrievals (quality flag $q_a \geq 0$) over the analyzed domain per orbit. The data from these orbits have been regridded and averaged at a resolution of $0.1° \times 0.1°$. A negative correlation of − 0.68 was found between the averaged XCH_4 and aerosol optical thickness (AOT). A linear regression between XCH_4 and AOT (Fig. S6D) yields a slope of − 364 ppb per unit of AOT, which has also been used to account for the influence of aerosols on the XCH_4 retrieval as a sensitivity study.

The uncertainty in TROPOMI-inferred emissions was represented by one standard deviation across an ensemble of estimates and in wind speed, and calculated as sum in quadrature. The ensemble of estimates was created by varying the following parameters: (a) background, varied at an interval of 0.25 (times length of source box) till the dimension length equals the length of the source box, (b) the regridding resolution, perform the analysis at different resolution $0.01° \times 0.01°$, $0.05° \times 0.05°$ and $0.1° \times 0.1°$, and (c) lastly vary the source box from $0.2° \times 0.2°$ to $0.7° \times 0.7°$ to test the influence of anthropogenic emissions on our estimate for Lusi (shown in Fig. S5). Finally, the uncertainties in wind speed were accounted by considering average winds over the source boxes at different time steps (0600 UTC h ± 2) and the variability in the winds over different source box. The uncertainties (one standard deviation) in wind speed is tabulated in the "Supplementary Material" (Table S1). Further details about the quantification of emission using TROPOMI data can be found in the "Supplementary Material".

Data availability

All data generated or analysed during this study are included in this published article and its "Supplementary Material" files. ECMWF ERA-5 reanalysis data is freely available at https://cds.climate.copernicus.eu. TROPOMI data can be accessed at Copernicus Open Access Hub (https://scihub.copernicus.eu/).

Received: 24 March 2020; Accepted: 2 February 2021
Published online: 18 February 2021

References

1. Shindell, D. T. *et al.* Improved attribution of climate forcing to emissions. *Science* **326**, 716–718 (2009).
2. Ciais, P. *et al.* In *Climate Change 2013: The Physical Science Basis. Contribution of Working Group I to the Fifth Assessment Report of IPCC* (eds T.F. Stocker et al.) 465–570 (Cambridge University Press, Cambridge, United Kingdom and New York, NY, USA, 2013).
3. Saunois, M. *et al.* Variability and quasi-decadal changes in the methane budget over the period 2000–2012. *Atmos. Chem. Phys.* **17**, 11135–11161 (2017).
4. Lassey, K. R., Etheridge, D. M., Lowe, D. C., Smith, A. M. & Ferretti, D. F. Centennial evolution of the atmospheric methane budget: What do the carbon isotopes tell us?. *Atmos. Chem. Phys.* **7**, 2119–2139 (2007).
5. Schwietzke, S. *et al.* Upward revision of global fossil fuel methane emissions based on isotope database. *Nature* **538**, 88–91 (2016).
6. Etiope, G., Ciotoli, G., Schwietzke, S. & Schoell, M. Gridded maps of geological methane emissions and their isotopic signature. *Earth Syst. Sci. Data* **11**, 1–22 (2019).
7. Hmiel, B. *et al.* Preindustrial $^{14}CH_4$ indicates greater anthropogenic fossil CH_4 emissions. *Nature* **578**, 409–412 (2020).
8. Etiope, G. & Schwietzke, S. Global geological methane emissions: An update of top-down and bottom-up estimates. *Elem. Sci. Anth.* **7**, 47. https://doi.org/10.1525/elementa.1383 (2019).
9. Dimitrov, L. I. Mud volcanoes—The most important pathway for degassing deeply buried sediments. *Earth Sci. Rev.* **59**, 49–76 (2002).
10. Milkov, A. V., Sassen, R., Apanasovich, T. V. & Dadashev, F. G. Global gas flux from mud volcanoes: A significant source of fossil methane in the atmosphere and the ocean. *Geophys. Res. Lett.* **30**(2), 1037 (2003).
11. Klusman, R. W., Jakel, M. E. & LeRoy, M. P. Does microseepage of methane and light hydrocarbons contribute to the atmospheric budget of methane and to global climate change? *Assoc. Pet. Geochem. Explor. Bull.* **11**, 1–55 (1998).
12. Etiope, G. & Klusman, R. W. Microseepage in drylands: Flux and implications in the global atmospheric source/sink budget of methane. *Glob. Planet. Change* **72**, 265–274 (2010).
13. Judd, A. G. Natural seabed seeps as sources of atmospheric methane. *Environ. Geol.* **46**, 988–996 (2004).
14. Kvenvolden, K. A. & Rogers, B. W. Gaia's breath—Global methane exhalations. *Mar. Pet. Geol.* **22**, 579–590 (2005).
15. Anthony, K. M. W., Anthony, P., Grosse, G. & Chanton, J. Geologic methane seeps along boundaries of Arctic permafrost thaw and melting glaciers. *Nat. Geosci.* **5**, 419–426 (2012).
16. Thornton, B. F. *et al.* Shipborne eddy covariance observations of methane fluxes constrain Arctic sea emissions. *Sci. Adv.* **6**(5), eaay7934 (2020).
17. Van Noorden, R. Mud volcano floods Java. *Nature* https://doi.org/10.1038/news060828-1 (2006).
18. Mazzini, A., Etiope, G. & Svensen, H. A new hydrothermal scenario for the 2006 Lusi eruption, Indonesia. Insights from gas geochemistry. *Earth Planet. Sci. Lett.* **317**, 305–318 (2012).
19. Procesi, M., Ciotoli, G., Mazzini, A. & Etiope, G. Sediment-hosted geothermal systems: Review and first global mapping. *Earth Sci. Rev.* **192**, 529–544 (2019).
20. Mazzini, A. *et al.* Triggering and dynamic evolution of the LUSI mud volcano, Indonesia. *Earth Planet. Sci. Lett.* **261**, 375–388 (2007).

21. Mazzini, A. *et al.* Strike-slip faulting as a trigger mechanism for overpressure release through piercement structures. Implications for the Lusi mud volcano, Indonesia. *Mar. Petrol. Geol.* **26**, 1751–1765 (2009).
22. Moscariello, A. *et al.* Genesis and evolution of the Watukosek fault system in the Lusi area (East Java). *Mar. Pet. Geol.* **90**, 125–137 (2018).
23. Sciarra, A. *et al.* Radon and carbon gas anomalies along the Watukosek Fault System and Lusi mud eruption, Indonesia. *Mar. Petrol. Geol.* **90**, 77–90 (2018).
24. Richards, J. R. Report into the past, present, and future social impacts of Lumpur Sidoarjo. *Tech. Rep. Humanitus Sidoarjo Fund,* Humanitus, Suarabaya, Indonesia. 162 pp (2011).
25. Karyono, K. *et al.* Lusi, a clastic-dominated geysering system in Indonesia recently explored by surface and subsurface observations. *Terra Nova* **29**, 13–19 (2017).
26. Vanderkluysen, L., Burton, M. R., Clarke, A. B., Hartnett, H. E. & Smekens, J. F. Composition and flux of explosive gas release at LUSI mud volcano (East Java, Indonesia). *Geochem. Geophys. Geosyst.* **15**, 2932–2946 (2014).
27. Mazzini, A., Scholz, F., Svensen, H. H., Hensen, C. & Hadi, S. The geochemistry and origin of the hydrothermal water erupted at Lusi, Indonesia. *Mar. Petrol. Geol.* **90**, 52–66 (2018).
28. Malvoisin, B., Mazzini, A. & Miller, S. A. Deep hydrothermal activity driving the Lusi mud eruption. *Earth Planet. Sci. Lett.* **497**, 42–49 (2018).
29. Svensen, H. H., Iyer, K., Schmid, D. W. & Mazzini, A. Modelling of gas generation following emplacement of an igneous sill below Lusi, East Java, Indonesia. *Mar. Petrol. Geol.* **90**, 201–208 (2018).
30. Zaputlyaeva, A., Mazzini, A., Caracausi, A. & Sciarra, A. Mantle-derived fluids in the East Java Sedimentary Basin, Indonesia. *J. Geophys. Res. Solid Earth* **124**, 7962–7977 (2019).
31. Zaputlyaeva, A. *et al.* Recent magmatism drives hydrocarbon generation in north-east Java, Indonesia. *Sci. Rep.* **10**, 1786 (2020).
32. Fallahi, M. J., Obermann, A., Lupi, M., Karyono, K. & Mazzini, A. The plumbing system feeding the Lusi eruption revealed by ambient noise tomography. *J. Geophys. Res. Solid Earth* **122**, 8200–8213 (2017).
33. Mauri, G. *et al.* Insights on the structure of Lusi mud edifice from land gravity data. *Mar. Pet. Geol.* **90**, 104–115 (2018).
34. Panzera, F. *et al.* Lusi hydrothermal structure inferred through ambient vibration measurements. *Mar. Pet. Geol.* **90**, 116–124 (2018).
35. Lupi, M. *et al.* Enhanced hydrothermal processes at the new-born Lusi eruptive system, Indonesia. *J. Volcanol. Geoth. Res.* **366**, 47–57 (2018).
36. Collignon, M., Schmid, D. W., Galerne, C., Lupi, M. & Mazzini, A. Modelling fluid flow in clastic eruptions: Application to the Lusi mud eruption. *Mar. Pet. Geol.* **90**, 173–190 (2018).
37. Burton, M. R., Sawyer, G. M. & Granieri, D. Deep carbon emissions from volcanoes. *Rev. Mineral. Geochem.* **75**, 323–354 (2013).
38. Morner, N. A. & Etiope, G. Carbon degassing from the lithosphere. *Glob. Planet. Change* **33**, 185–203 (2002).
39. Werner, C. *et al.* Carbon dioxide emissions from subaerial volcanic regions: Two decades in review. In *Deep Carbon: Past to Present* (eds. B.N. Orcutt, I. Daniel, & R. Dasgupta) 188–236 (Cambridge University Press, 2019).
40. Varon, D. J. *et al.* Satellite discovery of anomalously large methane point sources from oil/gas production. *Geophys. Res. Lett.* https://doi.org/10.1029/2019GL083798 (2019).
41. Jacob, D. J. *et al.* Satellite observations of atmospheric methane and their value for quantifying methane emissions. *Atmos. Chem. Phys.* **16**, 14371–14396 (2016).
42. Zhang, Y. *et al.* Quantifying methane emissions from the largest oil-producing basin in the United States from space. *Sci. Adv.* **6**, eaaz5120 (2020).
43. Pandey, S. *et al.* Using satellite data to identify the methane emission controls of South Sudan's wetlands. *Biogeosci. Discuss.* **2020**, 1–31 (2020).
44. Buchwitz, M. *et al.* Satellite-derived methane hotspot emission estimates using a fast data-driven method. *Atmos. Chem. Phys.* **17**, 5751–5774 (2017).
45. Crippa, M. *et al.* Fossil CO_2 and GHG emissions of all world countries: 2019 report. in *Report, EUR 29849 EN, Publications Office of the European Union, Luxembourg, 2019*. ISBN 978-92-76-11100-9. JRC117610 (2019). https://doi.org/10.2760/687800.
46. van der Werf, G. R. *et al.* Global fire emissions estimates during 1997–2016. *Earth Syst. Sci. Data* **9**, 697–720 (2017).
47. Bloom, A. A. *et al.* A global wetland methane emissions and uncertainty dataset for atmospheric chemical transport models (WetCHARTs version 1.0). *Geosci. Model Dev.* **10**, 2141–2156 (2017).
48. Copernicus. Climate Change Service (C3S) (2017): ERA5: Fifth generation of ECMWF atmospheric reanalyses of the global climate. Copernicus Climate Change Service Climate Data Store (CDS). https://cds.climate.copernicus.eu/cdsapp#!/home. Accessed June 2019.

Acknowledgements

The work was funded by the European Research Council under the European Union's Seventh Framework Programme Grant agreement no. 308126 (LUSI LAB project, PI A. Mazzini). We acknowledge the support from the Research Council of Norway through its Centres of Excellence funding scheme, Project Number 223272 (CEED) and the HOTMUD project (288299). This research contains modified[48] Sentinel data for 2018 and 2019. PS and SP are funded through the GALES (Gas Leaks from Space) project (Grant 15597) by the Dutch Technology Foundation, which is part of the Netherlands Organisation for Scientific research (NWO). BPLS and PPLS personnel are thanked for their field support. Finally, we thank the editor and the numerous reviewers for their constructive comments that improved this manuscript.

Author contributions

A.M., A.S. and G.E. organized the structure of the manuscript. A.M., A.S. and A.H. performed the field measurements and organized the field expeditions and coordination. P.S., S.H. and S.P. performed the TROPOMI data processing and interpretation. All authors contributed to the data interpretation, manuscript writing and revision.

Competing interests

The authors declare no competing interests.

Additional information

Supplementary Information The online version contains supplementary material available at https://doi.org/10.1038/s41598-021-83369-9.

Correspondence and requests for materials should be addressed to A.M.

SUPPLEMENTARY MATERIAL

Relevant methane emission to the atmosphere from a geological gas manifestation

Adriano Mazzini[1], Alessandra Sciarra[2], Giuseppe Etiope[2,3], Pankaj Sadavarte[4,5], Sander Houweling[4,6], Sudhanshu Pandey[4], Alwi Husein[7]

[1]Centre for Earth Evolution and Dynamics (CEED), University of Oslo, Oslo, Norway.

[2]Istituto Nazionale di Geofisica e Vulcanologia, via di Vigna Murata 605, 00143 Rome, Italy

[3]Faculty of Environmental Science and Engineering, Babes Bolyai University, Cluj-Napoca, Romania

[4]SRON Netherlands Institute for Space Research, Earth Science Group (ESG), Utrecht, the Netherlands

[5]Department of Climate, Air and Sustainability, TNO, Utrecht, the Netherlands

[6]Department of Earth Sciences, Vrije Universiteit, Amsterdam, the Netherlands

[7]Pusat Pengendalian Lumpur Sidoarjo (PPLS), Suarabaya, Indonesia

Lusi is a Sediment-Hosted Geothermal System (SHGS). These systems[1], characterized by carbon dioxide (CO_2) of deep geothermal origin (thermometamorphic or mantle-derived), interact with CH_4-rich fluids in shallower sedimentary rocks, leading to a hybrid CH_4-CO_2 surface seepage system. SHGSs often feature muddy craters or bubbling pools and can be confused with, either mud volcanoes (sedimentary volcanism; [2]) or mere geothermal/volcanic emissions. The methane vented at Lusi is mainly thermogenic ($\delta^{13}C$ from -40 to -49 ‰), although a possible mixing with shallower microbial gas (resulting in $\delta^{13}C$: -51.8 ‰) was observed in the initial stages of Lusi's activity[3].

1. Degassing modality

Lusi is a complex and multiple degassing system, with different components and modalities of gas release from the ground. The recognition of the degassing components was a prerequisite to design and perform gas flux measurements (Table 1).

The main degassing zone, which is object of the present work, covers an area of ~7 km^2, framed by a 12 m tall embankment (Fig. 1A, 2A). This surface can be divided in three main sectors.

(a) The central part (defined as crater zone) hosts two large active vents. These are characterized by constant gas and mud breccia release resulting in tens of meters tall plumes composed respectively of: 98% aqueous vapour, 1.5% CO_2 and 0.5% CH_4;[3,4].

Drone thermal images showed the presence of two distinct hot zones that correspond precisely to the two active vents, where the most active bubbling occurs releasing deeper and hotter fluids [5]. A significant thermal effect around the main vent extends over a surface of 200 m^2, and about 80 m^2 for the secondary one. The main vent clearly defines a surface temperature pattern of concentric rings. The crater zone has the highest temperatures and is characterized by the constant activity of bursting bubbles that reach the size of several meters.

(b) A ~650 m diameter subcircular pond (>0.3 km^2) surrounds the active vents region. This pond, consisting of hot mud, is not accessible and hosts countless bubbling points, which vary in size from meters to decimetres scale and change position continuously together with the mud breccia flows that radially expand from the crater zone.

(c) The external region consists of dry walkable mud-breccia and is sheared by radial streams that flush the hot mud erupted from the vents. In this area three main degassing types could be identified: soil miniseepage, fractured zones, satellite seeps.

i) *Soil miniseepage*: a diffuse exhalation occurring throughout the walkable area inside the embankment, where no specific features are observed and mud appears to be generally undisturbed (Fig. 1A, 2C). It is analogous to “miniseepage” typically reported around seeps and mud volcanoes (e.g.; [6]).

ii) F*ractured zones:* characterized by ten to hundred meter long fissures, centimetres to several meters wide and up to 3-5 meters deep (Fig. 1A, 2B, S2). They were mapped combining direct

field observations and high resolution satellite images as well as drone photogrammetry. The main fractured/faulted zones are NE-SW oriented (i.e. part of the Watukosek strike slip fault system) or coincide with the system of antithetic fracture zones (Siring fault system)[7-10].

iii) S*atellite seep*s: active bubbling pools, broadly distributed throughout the entire region inside the embankment (Fig. 1A, 2D, S3). Seeps are circular depressions with an average diameter in the order of 20-30 cm, up to 1.5 m, and typically expel gas, water and, in some rare instances, mud, thus resulting in the formation of small gryphons. These seeps are part of an intricate subsurface plumbing system that continuously mutates in time as the fluids follow preferential pathways to reach the surface.

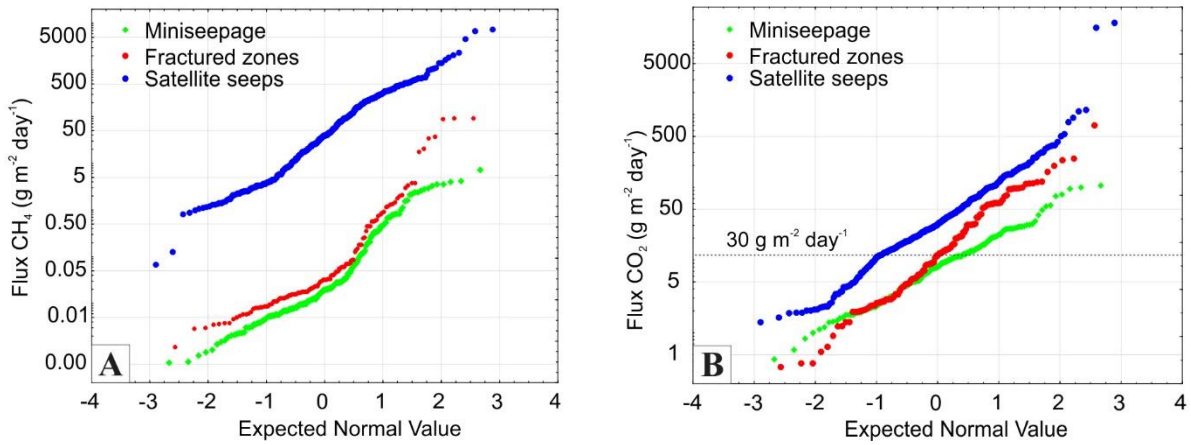

Fig. S1. *(A-B) Normal probability plots for CH_4 and CO_2 to define the background values and the anomalous populations. Note logarithmic scale of ordinate (y) axis.*

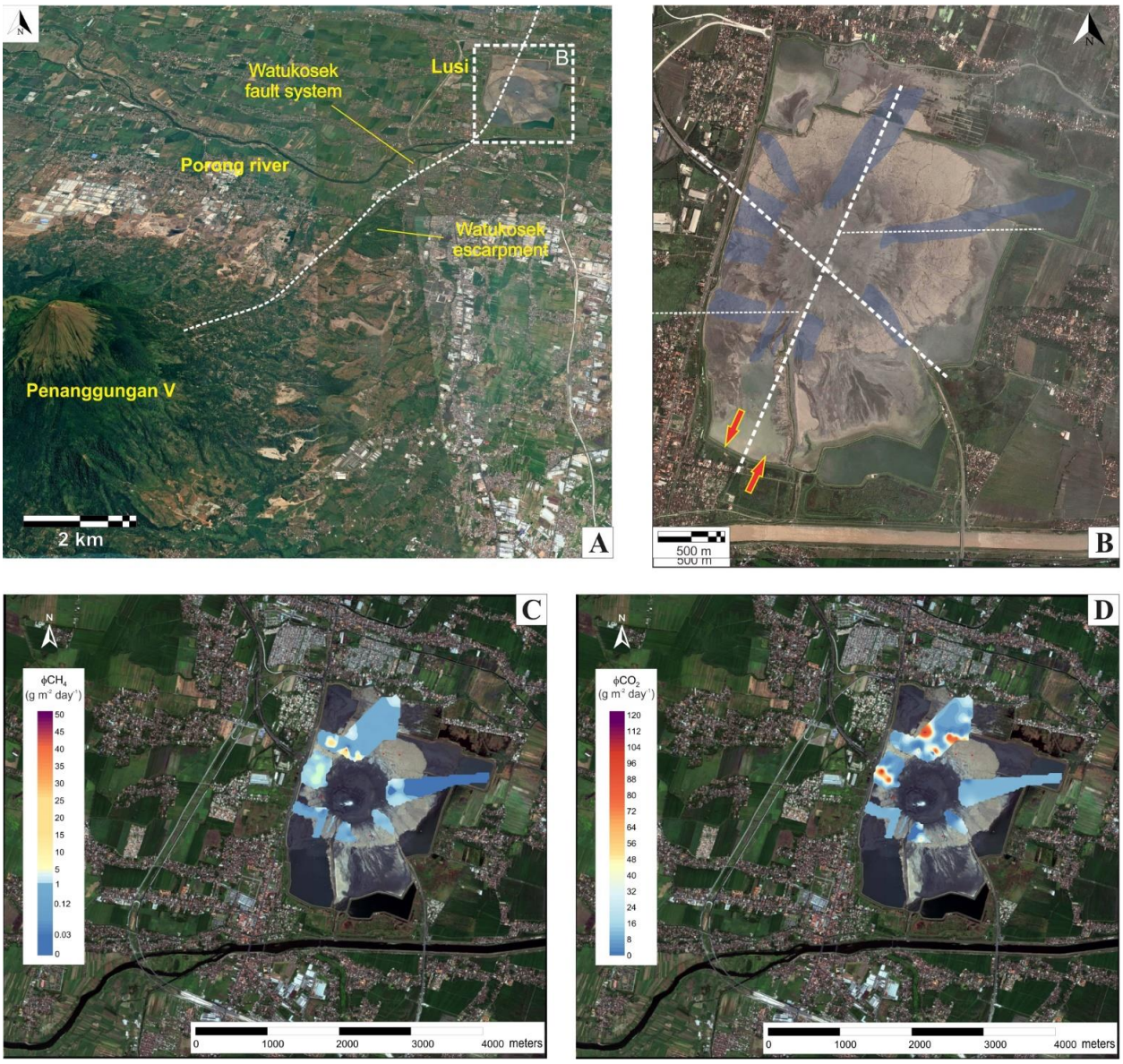

Fig. S2. *Fractured zones inside the embankment area. A) Google Earth satellite image of the region around Lusi. Indicated are the main features (moving towards the NE: Penanggungan volcano of the Arjuno-Welirang volcanic complex, the fault outcrop of the Watukosek escarpment, the bent path of the Porong River and the intersection with Lusi); (B) High resolution Ikonos satellite image and details of the fractured and faulted area inside the Lusi embankment based on field and satellite observations. Grey shaded areas indicate the zones with high amount of fractures, dashed lines trace the direction of the main and the antithetic fractures on field; (C-D) elaboration maps of CH_4 and CO_2 flux from the faulted areas. This figure has been constructed using Surfer 12.0 (Golden Sofware).*

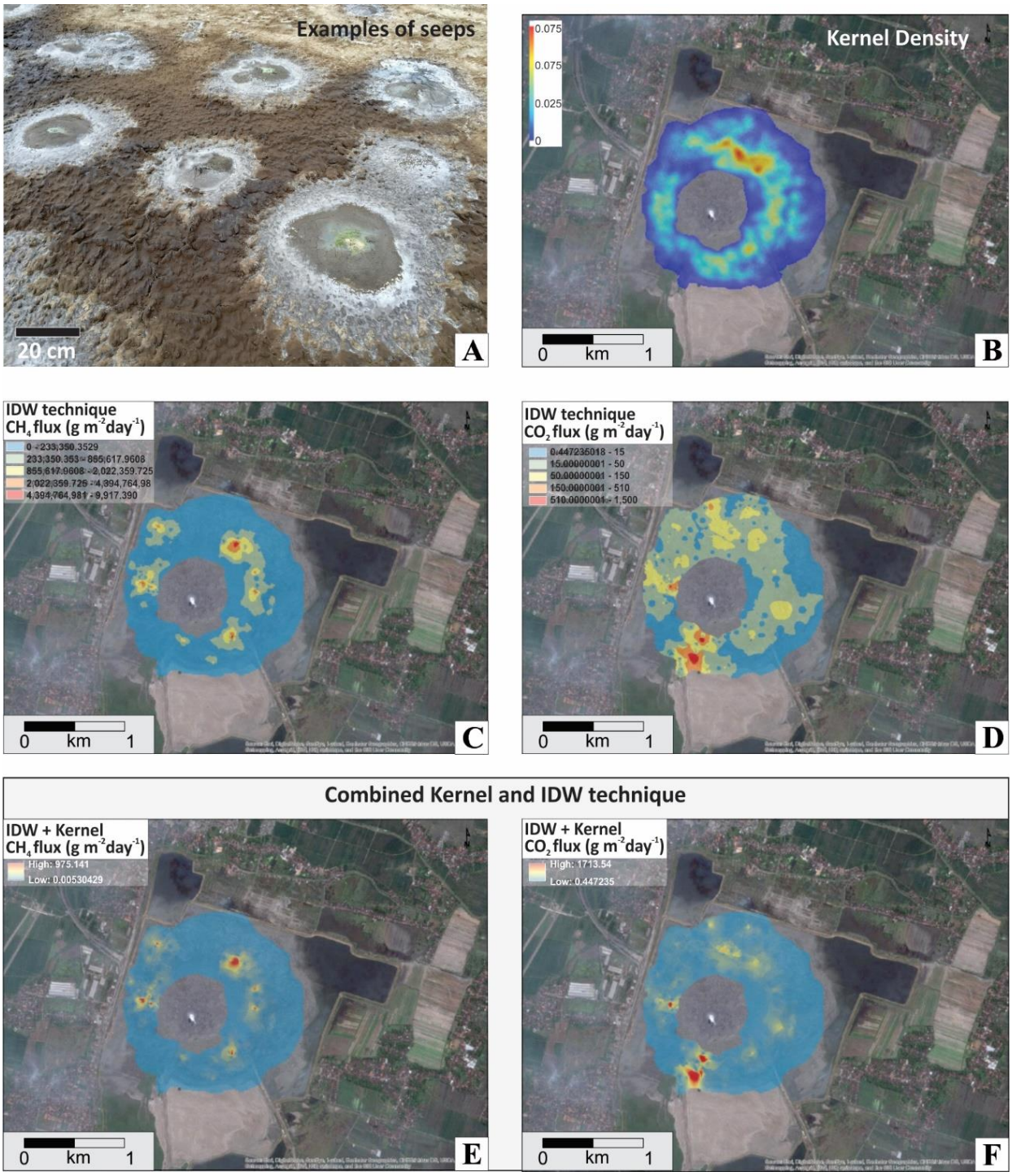

Fig. S3. *Satellite seeps inside the embankment area. A) Group of active seeps inside the embankment. (B) Superposed Ikonos satellite view and Kernel density; (C-D) Calculated CH_4 and CO_2 flux using IDW technique; (E-F) Combined Kernel and IDW technique for CH_4 and CO_2 fluxes. Basemap obtained using Statistica 10.0.*

2. Total emission estimates

Crater zone: The largest active vent (Vent 1) was monitored during its regular activity (i.e. excluding the powerful geysering events that characterize about half of the activity at Lusi; [11]). Between 2015-2019, a total of 205 replicated measurements were completed during low (< 1 m s^{-1}) wind conditions using a theodolite (Topcon AT-G2) positioned in the observatory tower located in the SE of the embankment zone (Fig. 1A, 2A). It was then measured the time required for a beamed point of the vapour plume of the main vent to move from a given height A to another height B. This large database shows that the speed of the rising plume ranges from 0.4 to 1.5 m/s (Fig. S4A). The resulting average speed of the plume is 0.86 m s^{-1} (± 0.19 m/s standard deviation). Based on comparative satellite and drone images we estimated that the main vent has a diameter of ~100 m. However, observations show that during the regular Lusi activity a) the plume does not occupy the full width of the vent but rather its central area (width of ~50 m, Fig. 1C) and b) the plume density is not homogeneous throughput its volume and contains air pockets. Our conservative estimates consider that the plume has air content ranging between 70-80% (Fig. S4B).

Monitoring of the smaller vent (Vent 2) shows that its behaviour is similar to that of the larger one. A diameter of 35 m was selected with the same parameters used for the main vent. These conservative parameters (i.e. 50 and 35 m wide plumes, 20-30% gas volume, regular vent activity) were then used for calculations. The crater gas composition was calculated from a large sample suite that we collected directly from the crater since 2006 in agreement with the values measured by Vanderkluysen et al.[4]. We know that 98 vol.% of Lusi plume is composed by aqueous vapour, while the remaining ~2 vol.% consists of CO_2 (respectively 1.49 vol.%) and CH_4 (0.51 vol.%)[3,4].

The total amount of gas released inside the gas plume has been estimated as follow:

$$G_i = \rho_i \left[\alpha_i \left(v \cdot S \right) \right]$$

Where G_i is the mass flux of a specific gas i (CO_2 or CH_4); ρ_i is the density of the gas; α_i is the concentration of this gas in the total volume flux of the plume; v is the velocity in the plume (0.86±0.19 m/s) of cross-sectional area S (1962 m^2 for main vent and 1017m^2 for smaller vent). The gas density can be estimated using molar volume of the ideal gas at 1 atm and 40º C (V_m=25.696 l/mol) and molar mass (M_{CO2}=44 g/mol and M_{CH4}=16 g/mol) as $\rho_i = M_i/V_m$. The gas

concentration α_i is the product of gas concentration from the crater (0.01492 for CO_2 and 0.00508 for CH_4) and the concentration of crater gas within the air-polluted plume (0.25 ± 0.05). Using this method we estimate a total flux from the main vent of ~42 ktonnes CH_4 yr^{-1}, and ~ 339.5 ktonnes CO_2 yr^{-1} while the second vent emits ~ 21.8 ktonnes CH_4 yr^{-1}, and ~176 ktonnes CO_2 yr^{-1}.

Miniseepage and fracture zones: The data treatment of flux measurements on miniseepage and fractured zones involved the calculation of standard statistical parameters. The Sinclair method[12] was applied to define background values by means of normal probability plot (NPP). As suggested by Fig. S1A, the probability plots of ϕCH_4 (logarithmic positive values) confirm that flux values have a log-normal distribution and highlight the presence of two different populations both for miniseepage and fractured zones. Differently, most ϕCO_2 variations (Fig. S1B) can be ascribed to a single population, with the exception of the background value (30 g m^{-2} day^{-1}) and some outliers with $\phi CO_2 \geq 200$ g m^{-2} day^{-1}, likely related to the occurrence of fractures causing an increased soil permeability at a local scale.

Moreover, in order to estimate a background value of the regional flux and its expected gradual decrease furthering from the crater zone, several profiles have been extended up to 2.7 km outside the embankment zone (Fig. 2A). The CO_2 weighted average was calculated taking into account only the measurements above the background values (30 g m^{-2} day^{-1}), likely dominated by biological soil respiration, while for CH_4 all positive measured values were considered (Fig. S1A-B).

Miniseepage and fractured zones statistical elaboration allows to estimate the gas emission rates (expressed in tonnes day^{-1}) by Natural Neighbour interpolation and volume method. In particular, a total of 175 flux measurements were carried out to estimate the miniseepage emission type. At any of these localities flux of CO_2 and CH_4 was detected resulting in mean values of 13.07 g m^{-2} day^{-1} (ϕCO_2) and 361 mg m^{-2} day^{-1} (ϕCH_4). This value has been applied for all the area framed by the embankment interested by miniseepage (5.91 km^2) resulting in a total average flux of 2.01 (from 1.3 to 4.8 lower and upper quartile, respectively) tonnes day^{-1} of CO_2 and 2.12 (from 0.9 to 5.6 lower and upper quartile, respectively) tonnes day^{-1} of CH_4.

The 129 flux measurements completed in the fractured regions (Fig. S2) revealed a CO_2-dominated seeping gas and have significantly higher soil temperatures and flux rates compared with the

surrounding undisturbed sediments. The calculated mean values are 35.75 g m^{-2} day^{-1} and 3.22 mg m^{-2} day^{-1} for ϕCO_2 and ϕCH_4, respectively. These values have been applied for the mapped fractured zones (1.34 km^2) resulting in a total average flux of 47.90 (from 15 to 100 lower and upper quartile, respectively) tonnes day^{-1} of CO_2 and 4.31 (from 0.04 to 19 lower and upper quartile, respectively) tonnes day^{-1} of CH_4. Fractured zones also show high concentration of active seeps confirming a greater amount of fluids release at these localities.

Satellite seeps: The average calculated flux rate among the 351 measured seeps is 71.68 g m^{-2} day^{-1} of CO_2 and 218.31 g m^{-2} day^{-1} of CH_4. The amount of CH_4 and CO_2 released by the satellite seeps was obtained by adding together the individual contribution of each measured seep.

Since the amount of satellite seeps occurring inside the embankment largely exceed the amount of those measured, the position of all the seeps was digitized based on high resolution satellite images. Their location can be easily recognized due to the colour contrast between the dry and the water-saturated sediments (Fig. S3A). Normal probability plots were used to calculate the population classes of the measured fluxes. The emission factor for CO_2 and CH_4 is the result of the weighted average for every single population class and the mean of the weighted averages of all the identified classes. These emission factors were applied for the number of seeps (total of 16,148) that have been mapped from the high resolution satellite images (Fig. 1A). Moreover, an additional statistical procedure was then applied in order to estimate the amount of CO_2 and CH_4 outgassing from these digitized seeps (i.e. defined as "points" in the following) but not measured in situ. The procedure combines the following statistical processing: *i)* Natural Neighbour that interpolates a raster surface from points using a natural neighbour technique; *ii)* IDW that interpolates a raster surface from points using an inverse distance weighted (IDW) technique; *iii)* Kernel Density that calculates a magnitude per unit area from point or polyline features using a Kernel function to fit a smoothly tapered surface to each point or polyline; *iv)* Raster Calculator that builds and executes a single Map Algebra expression using Python syntax in a calculator-like interface.

More details and references about these processing procedures are provided below. Natural Neighbour technique is a common and robust interpolation method that produces a conservative and artifice-free result. This approach aims to find, among the samples, the closest subset to each interpolation point and then applies weighted averages on them based on proportionate areas to

interpolate a value[13-16]. The interpolated surface is tightly controlled by the original data points and has the advantage of not having to specify parameters such as radius, number of neighbours or weights. The use of this method is most appropriate where sample data points are distributed with uneven density. The Inverse Distance Weighted (IDW) technique is an interpolation method usually applied to highly variable data assuming that each input point (i.e., digitized filtrations) has a local influence that decreases with distance. The use of this method assumes that the closer points have a greater weight than those further away and therefore their influence decreases with the distance from their sampled position[17-21]. Kernel density estimation is a statistical tool that allows to create a smooth curve given a set of data and to visualize the "shape" of some data, as a kind of continuous replacement for the discrete histogram[22-24]. Conceptually, a smoothly curved surface is fitted over each point. The surface value is highest at the location of an analysed point and diminishes with increasing distance ultimately reaching zero at the search radius distance (defined as 2 m based on concentric measurements conducted around a set of reference seeps) from the point. The digitalized seeps were analyzed and integrated using Raster Calculator to estimate and map their distribution in the study area[25-28].

The final product results from the merged Kernel and IDW maps (Fig.S3 B-F). A total flux of 14.59 and 98.52 tonnes day^{-1} of CO_2 and CH_4, respectively, was therefore calculated for all the seeps within the embankment.

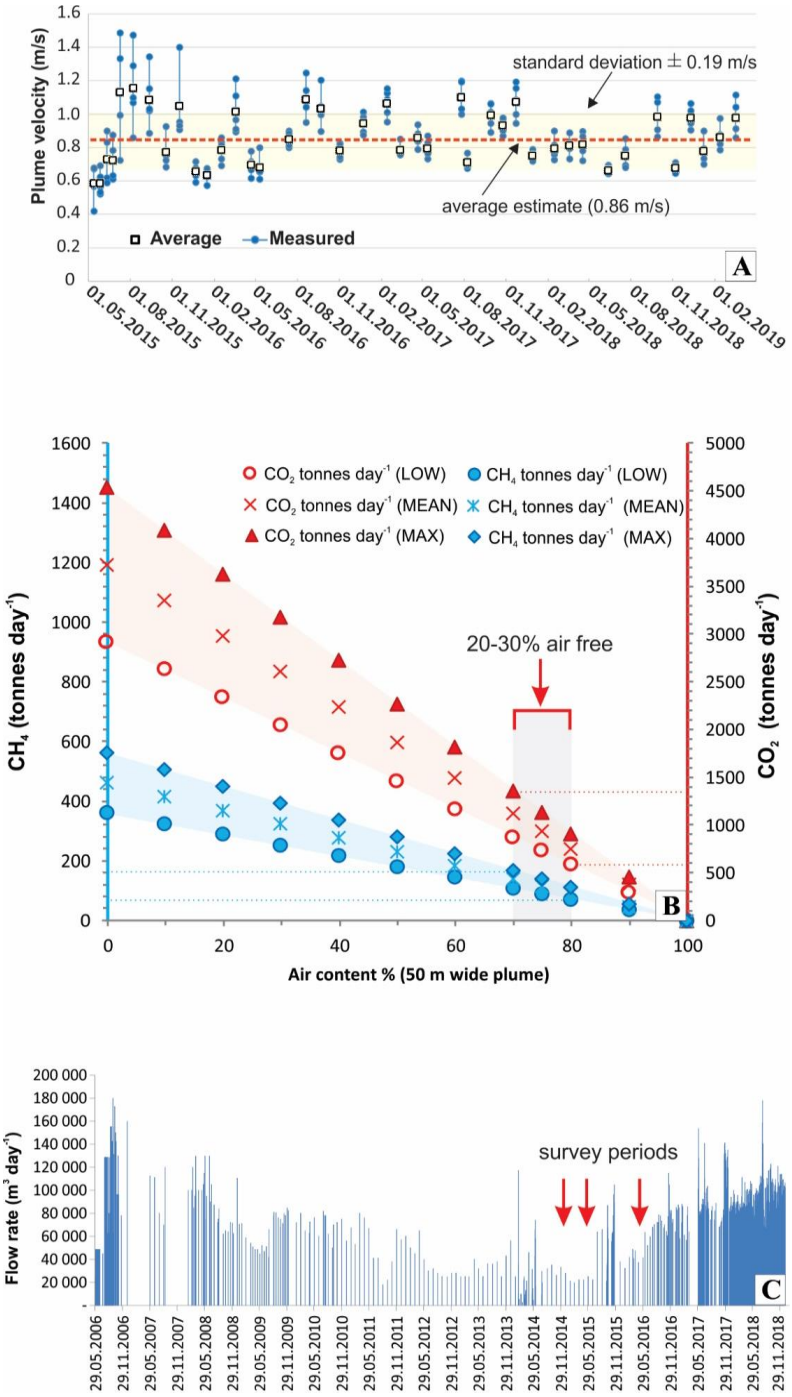

Fig. S4. *(A) Measured plume velocities since May 2015-March 2019. Indicated with the red line the average value calculated from the 205 measurements; shaded area indicates the standard deviation used for calculations. (B) Plot of daily CO_2 and CH_4 discharge from a 50 m wide plume during its regular activity. Considering a conservative gas content in the plume (i.e. between 20-30%) the daily flux is estimated to vary between 583-1358 tonnes day^{-1} of CO_2 and 72-168 tonnes day^{-1} of CH_4. (C) Mud flow rate measured since Lusi inception.*

3. Mud flow rate

Since the Lusi inception in May 2006, different approaches have been used to estimate the mud flow rate (Fig. S4C). Some of these methods are linked to the continuously mutating field conditions, the size of the eruption site, and the contingency procedures required to mitigate potential hazardous situations. These field operations were either combined or modified through time and had to be all taken into account in order to obtain the total flow rate (see more details in [29]). During the initial phases, the mud flow extension was monitored using satellite images and a portion of the erupted mud was scooped and loaded into large trucks so it could be removed, treated, and dumped at selected locations. In parallel several framed ponds were built around the crater zone to protect the settlements and control the spreading of the mudflows. The surface of these ponds was calculated using multiple IKONOS satellite images as well as measuring their empty volume. The flow rate within these ponds was then monitored using calibrated sticks. Since 2006 the region has been constantly monitored by a dense GPS network in order to measure potential subsidence in the area, and the flow rate estimates were compensated with recorded vertical movements[29]. Since October 2006, the erupted mud was treated and discharged, through a system of pumps, to the Porong River located to the south and later, in much lesser volumes, also to the stream located to the north of Lusi. Since March 2009 the active vent remained isolated at the centre of the large embankment zone and the erupted mud was forced towards the south to optimize the flushing into the Prong River. In order to implement the removal of clasts and fine-grained sediments deposited in the outskirts of the embankment zone, a “circular” pumping system strategy was applied when needed. First, water from the Porong River was pumped inside the outermost sectors of the embankment area; these newly created pools were then dredged in order to stir up in suspension the solid particles and ultimately pump all the sediment-enriched mixture out into the Porong River. The flow rate calculations were compensated with the amount of fresh water pumped inside these pools. All the estimates were compensated by the measured precipitations. Considering the significant amount of water evaporation that occurs directly at the crater site, in the surrounding large pond, and in the remaining area inside the embankment, the flow estimates might represent a lower value than the one reported herein.

4. TROPOMI - Emission quantification using the source pixel method

The TROPOMI instrument onboard the European Space Agency's Sentinal-5P satellite was launched in October 2017. The satellite is in a sun-synchronous orbit with a local overpass time of 13:30 hours. It has a wide swath of 2600 km and provides column averaged CH_4 mixing ratios (XCH_4), among other species, at ~7×7 km^2 ground pixel resolution at nadir and near daily global coverage. We analyzed data collected between May 2018 and July 2019 for local enhancements in XCH_4 over Lusi to provide an independent quantification of methane emissions and compare it with the estimates derived from in-situ measurements.

We use the mass balance method, described in Buchwitz et al.[30], to quantify the methane emission from Lusi. The mass balance method has the advantage that it is a quick method and does not require an atmospheric transport model. However, the method makes simplistic assumptions about the CH_4 emission distribution and atmospheric transport. In this method, the source flux Q [Gg y^{-1}] is calculated by multiplying the ΔXCH_4 enhancement (XCH_4 *source* – XCH_4 *background*) with a conversion factor CF shown below:,

$$Q = \Delta XCH_4 \times CF$$

$$CF = L \times V \times M_{exp} \times M \times C$$

where L *[km]* is the effective length of the source area through which the air parcel carrying methane is ventilated (computed as square root of the source region), V *[km* h^{-1}*]* is the effective wind speed, M_{exp} is the ratio of average surface pressure in the source box and standard surface pressure of 1013.25 hPa, M is a constant to convert concentration to mass change per area *[5.345 kg* CH_4 km^{-2} ppb^{-1}*]* in standard atmospheric conditions and C is a dimensionless factor chosen to be 2.0, derived by Buchwitz et al.[30], based on the concentration difference of the air parcel before and after entering the source area.

The domain of the TROPOMI analysis ranges from 6.027 to 9.027 °S latitude and 111.211 to 114.211 °E longitude (Fig. S5).

The source box 1 (see Fig. S5) covers a rectangular area of ~20×20 km^2 centered around the Lusi eruption site located at 112.711 ^{o}E, 7.527 ^{o}S. To calculate the XCH_4 enhancement in the source box, the local background mixing ratio in the upwind direction of the source pixels is subtracted. The local background region is chosen in upwind direction of the source box, with the dimension equal to the length of the source box, which lies to the East and South-East of Lusi given the

dominant wind direction during the analyzed period (see Fig S6A). The spatial distribution of XCH_4 is corrected for the influence of variations in surface elevation by adding 7 ppb/km relative to mean sea level[30]. Boundary layer averaged wind fields from ECMWF ERA5 are used, representing the 06:00 UTC overpass time of TROPOMI (C3S, 2017). Figure S6B shows the wind speed and direction for each grid pixel of ECMWF ERA5 winds over the domain from all the considerable days of the screened orbits. Since the selected source box is larger than the area of Lusi (~7 km^2), other sources may be present. To account for their contribution, anthropogenic emissions from EDGAR v5.0 for 2015;[31], biomass burning emissions from the GFED4.1s emission inventory for 2018;[32] and wetland emissions from WetCHARTs version 1.0;[33] for 2015 were subtracted. Emissions were quantified for boxes 1-6 (Fig. S5), with varying contributions from anthropogenic emissions to test the robustness of the emission estimate for Lusi.

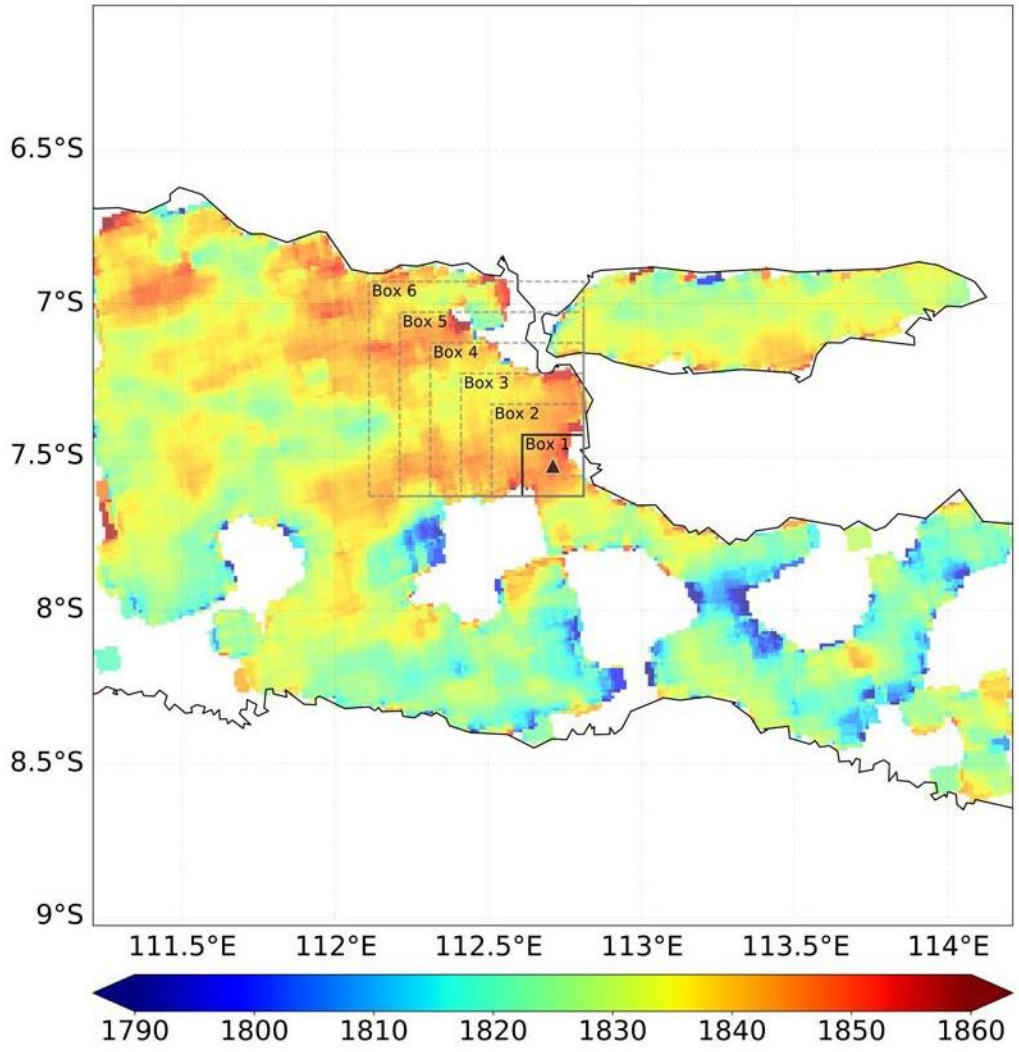

Fig. S5. *An oversampled (0.01° × 0.01°) map of TROPOMI data averaged over the study domain from May 2018 till July 2019. The location of Lusi is indicated by a triangle and the squares denotes the multiple source boxes considered for emission quantification. Units in ppb. Map generated using Python 2.7.13 version.*

Case for sensitivity: Data averaging and bias correction

A total of 50 orbits were screened for data availability, in the period May 2018 – July 2019 requiring > 100 pixels per orbit, to have sufficient spatial coverage over the domain. Figure S6C show the temporal spread of screened orbits across the analysis period. The data in these orbits

were regridded and averaged at a resolution of 0.1° × 0.1°. The selected orbits show a significant correlation between XCH_4 and aerosol optical thickness (AOT) varying from -0.13 to -0.86, with a correlation of -0.68 averaged over all data. The averaged data were corrected to remove this correlation by linear regression between XCH_4 and AOT (Fig. S6D), yielding a slope of -364 ppb per unit of AOT. As a sensitivity test, emissions were quantified using TROPOMI data including and excluding this additional bias correction.

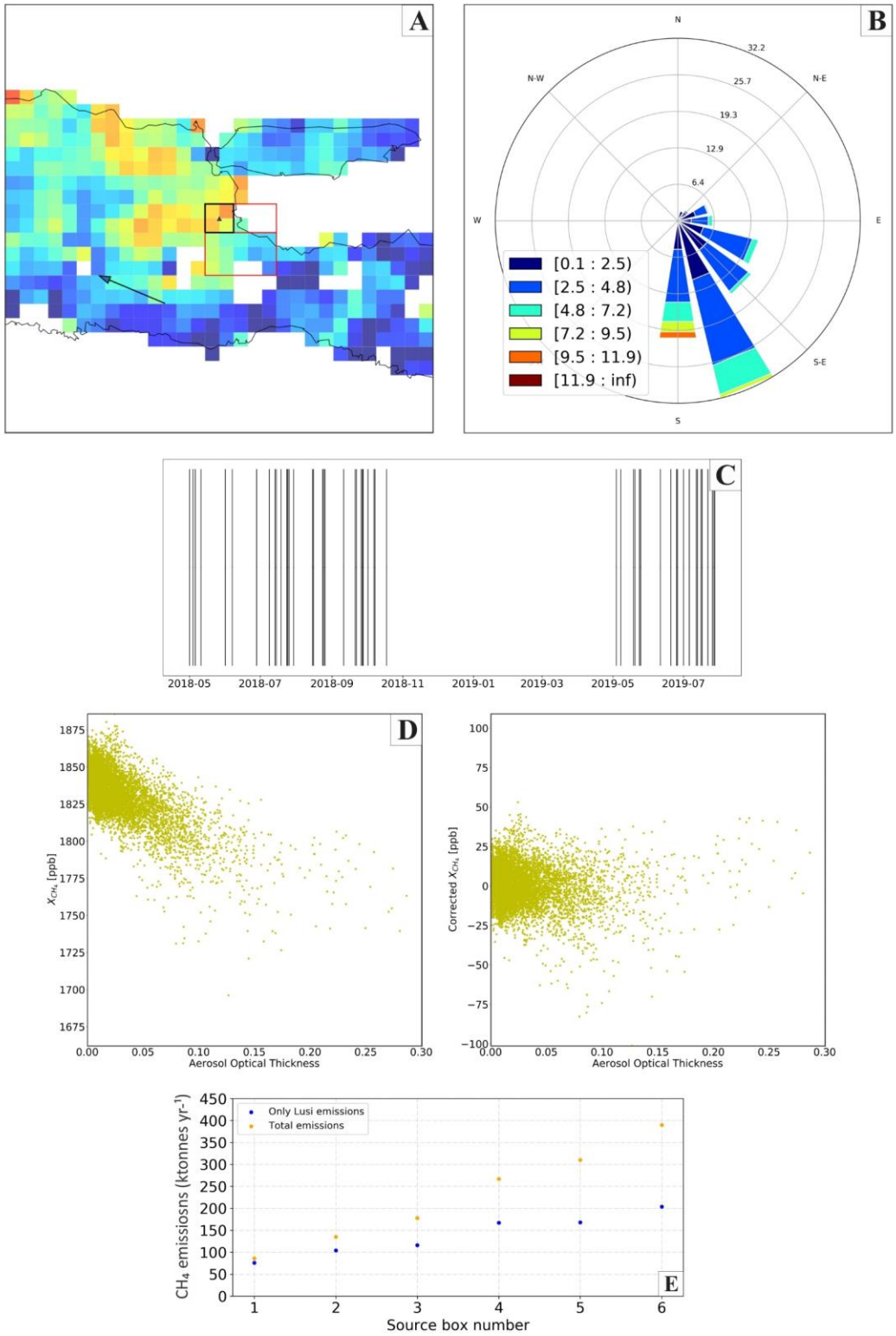
A
B
N
N-E
E
S-E
S
W
N-W
32.2
25.7
19.3
12.9
6.4
[0.1 : 2.5)
[2.5 : 4.8)
[4.8 : 7.2)
[7.2 : 9.5)
[9.5 : 11.9)
[11.9 : inf)
C
2018-05
2018-07
2018-09
2018-11
2019-01
2019-03
2019-05
2019-07
D
X_{CH_4} [ppb]
Aerosol Optical Thickness
Corrected X_{CH_4} [ppb]
Aerosol Optical Thickness
E
Only Lusi emissions
Total emissions
CH_4 emissiosns (ktonnes yr^{-1})
Source box number

Fig. S6. *Mass balance method defining regions, bias correction and final estimates for TROPOMI. (A) Local background region (red polygon) as defined in the upwind direction of source box (black polygon) for TROPOMI measurements. The dominant wind direction is arrowed. (B) Windrose diagram showing dominant wind speed and wind direction from all the grids of considered orbits (domain: 112.711 ± 0.525, -7.527 ± 0.525). (C) Screened orbits considered for the analysis spread across different months in 2018-2019. On the x-axis we have the temporal scale and each vertical line along y-axis represents screened orbit considered for the analysis. (D) The relation between TROPOMI XCH_4 and AOT before (left panel) and after (right panel) correction using linear regression. (E) Methane emissions quantified from TROPOMI data using source boxes increasing in size (see Fig. S5 for the definition of box 1-6). Total emissions include emissions from Lusi, EDGARv5.0 anthropogenic, GFED4.1s biomass burning and wetlands. All images were generated using Python 2.7.13 version.*

CH_4 emission from Lusi

In this study, we use the official TROPOMI operational two-band retrieval product. It uses the O_2A band at 0.79 μm and the CH_4 band at 2.3 μm in respectively the NIR and SWIR spectral bands of TROPOMI. XCH_4 is retrieved using the full-physics RemoTeC algorithm, accounting for light path perturbations due to scattering on aerosol and cirrus cloud particles in the atmosphere[34,35]. Butz et al.,[35] showed that XCH_4 from the full-physics retrieval algorithm used for TROPOMI data can have large errors over dark surfaces. This can affect our emissions estimates. Therefore, we filter out TROPOMI pixels with SWIR albedo of less than 0.02 (ATBD [36]). Using the mass balance approach outlined above, the CH_4 emission from Lusi was estimated at 140 ± 87 ktonnes yr^{-1}. This number is consistent with the independent estimate that is obtained from surface data, albeit that uncertainty margins are large. The sensitivity test using corrected data gave an estimate of 70 ktonnes yr^{-1}, which lies within the high uncertainty range of our estimate. Using the ensemble of estimates due to varying background, source box and regridding resolution we calculate an uncertainty of 60% around the quantified mean emission. For the wind speed, we estimate an uncertainty of 18% (around the mean) which is similar to that found in measurements i.e. 22% (0.19/0.86 m s^{-1}) (Figure S4A). Moreover, the surface data are expected to lead to a lower emission rate due to a low mud flow rate during the 2014-2016 in situ survey period (Fig S4C). The TROPOMI measurements where conducted for the period 2018-2019. During this time interval

mud flow rates were higher, with likely increased fluxes of water vapor, CO_2 and CH_4 (Fig. S4C). The high uncertainty in the TROPOMI-derived estimate is mainly due to the sensitivity to the choice of the background and source boxes. The anthropogenic emission from EDGARv5.0 varies between 10 ktonnes yr^{-1} and 184 ktonnes yr^{-1} while that of GFED4.1s varies between 0.09 to 0.41 ktonnes yr^{-1} and wetland varies from 0.04 to 1.65 ktonnes yr^{-1} going from ~20×20 km^2 to ~70×70 km^2, and therefore become significant at larger source box sizes. Further details about the estimates and other parameters are tabulated in Table S1. Our emission quantification method cannot clearly distinguish all sources of emissions in the vast region around Lusi. These could include unusually high anthropogenic sources (not identified so far on the basis of the information we got from maps and local authorities) and additional natural geological emissions such as the seepage activity that has been reported in the region (e.g. [37] and refs therein). In any case, the TROPOMI estimates are consistent with a significant source from Lusi for any choice of region (Fig. S6E).

Source region	Size (deg)	Dimension (Lat-Long) (deg)	Wind Speed (m/s)	Total mass balance (Gg/y)	EDGAR v5.0 (Gg/y)	GFED v4.1s (Gg/y)	Wetland (LPJ) (Gg/y)	Lusi (Gg/y)
Box 0	0.2° × 0.2°	(-7.427 : -7.627) (112.611 : 112.811)	1.36 ± 0.12	86	10.02	0.09	0.04	76 ± 24
Box 1	0.3° × 0.3°	(-7.327 : -7.627) (112.511 : 112.811)	1.52 ± 0.15	135	31.09	0.19	0.13	104 ± 30
Box 2	0.4° × 0.4°	(-7.227 : -7.627) (112.411 : 112.811)	1.42 ± 0.13	178	61.58	0.27	0.17	116 ± 33
Box 3	0.5° × 0.5°	(-7.127 : -7.627) (112.311 : 112.811)	1.76 ± 0.08	267	99.54	0.33	0.45	167 ± 61
Box 4	0.6° × 0.6°	(-6.977 : -7.627) (112.211 : 112.811)	1.56 ± 0.05	310	140.98	0.37	0.98	168 ± 56
Box 5	0.7° × 0.7°	(-6.927 : -7.627) (112.111 : 112.811)	1.87 ± 0.08	390	184.15	0.41	1.65	204 ± 68

Table S1: *Input parameters used to calculate methane emissions at Lusi eruption site for different source input.*

References

1 Procesi, M., Ciotoli, G., Mazzini, A. & Etiope, G. Sediment-hosted geothermal systems: Review and first global mapping. *Earth-Science Reviews* **192**, 529-544, (2019).

2 Mazzini, A. & Etiope, G. Mud volcanism: An updated review. *Earth-Science Reviews* **168**, 81–112, (2017).

3 Mazzini, A., Etiope, G. & Svensen, H. A new hydrothermal scenario for the 2006 Lusi eruption, Indonesia. Insights from gas geochemistry. *Earth and Planetary Science Letters* **317**, 305-318, (2012).

4 Vanderkluysen, L., Burton, M. R., Clarke, A. B., Hartnett, H. E. & Smekens, J. F. Composition and flux of explosive gas release at LUSI mud volcano (East Java, Indonesia). *Geochemistry Geophysics Geosystems* **15**, 2932-2946, (2014).

5 Di Felice, F., Mazzini, A., Di Stefano, G. & Romeo, G. Drone high resolution infrared imaging of the Lusi mud eruption. *Marine and Petroleum Geology* **90**, 38-51, (2018).

6 Etiope, G. Natural Gas Seepage. The Earth's hydrocarbon degassing. *Springer International Publishing Switzerland, ISBN 978-3-319-14601-0 (eBook), DOI 10.1007/978-3-319-14601-0.*, 199, (2015).

7 Mazzini, A. *et al.* Strike-slip faulting as a trigger mechanism for overpressure release through piercement structures. Implications for the Lusi mud volcano, Indonesia. *Marine and Petroleum Geology* **26**, 1751-1765, (2009).

8 Sciarra, A. *et al.* Radon and carbon gas anomalies along the Watukosek Fault System and Lusi mud eruption, Indonesia. *Marine and Petroleum Geology* **90**, 77-90, (2018).

9 Mauri, G. *et al.* Insights on the structure of Lusi mud edifice from land gravity data. *Marine and Petroleum Geology* **90**, 104-115, (2018).

10 Moscariello, A. *et al.* Genesis and evolution of the Watukosek fault system in the Lusi area (East Java). *Marine and Petroleum Geology* **90**, 125-137, (2018).

11 Karyono, K. *et al.* Lusi, a clastic-dominated geysering system in Indonesia recently explored by surface and subsurface observations. *Terra Nova* **29**, 13-19, (2017).

12 Sinclair, A. J. Selection of threshold values in geochemical data using probability graphs. *J. Geochem. Explor.* **3**, 129–149, (1974).

13 Watson, D. F. & Philip, G. M. Neighborhood-based interpolation. *Geobyte* **2**, 12–16, (1987).

14 Sibson, R. in *Interpreting Multivariate Data:* (ed V. Barnett) 21–36 (John Wiley & Sons, 1981).

15 Sambridge, M., Braun, J. & McQueen, H. Geophysical parameterization and interpolation of irregular data using natural neighbours. *Geophys. J. Int.* **122**, 837–857., (1995).

16 Bobach, T., Farin, G., Hansford, D. & Umlauf, G. Natural neighbor extrapolation using ghost points. *Computer aided design* **41**, 350-365, (2009).

17 Bartier, P. M. & Keller, C. P. Multivariate interpolation to incorporate thematic surface data using inverse distance weighting (IDW). *Computers & geosciences* **22**, 795-799, (1996).

18 Mueller, T. G. *et al.* Map Quality for Ordinary Kriging and Inverse Distance Weighted Interpolation. *Soil Science Society of America journal* **68**, 2042-2047, (2004).

19 Yang, W.-R., Wang, R.-S., Huang, J.-L., Chen, Z. & Li, F. Application of inverse distance weighted interpolation method in contaminated site assessment. *Ying Yong Sheng Tai Xue Bao* **18**, 2013, (2007).

20 Watson, D. F. & Philip, G. M. A refinement of inverse distance weighted interpolation. *Geo-Processing,* **2**, 315-327, (1985).
21 Setianto, A. & Triandini, T. Comparison of kriging and inverse distanceweighted (IDW) interpolation methods in lineament extraction and analyses. *Journal of Applied Geology* **5**, (2015).
22 Silverman, B. W. *Density estimation for statistics and data analysis*. (Chapman and Hall, 1986).
23 Scott, D. W. *Multivariate density estimation : theory, practice, and visualization*. (Wiley, 1992).
24 Węglarczyk, S. Kernel density estimation and its application. *ITM Web of Conferences 23, 00037 (2018) XLVIII Seminar of Applied Mathematics, https://doi.org/10.1051/itmconf/20182300037*, (2018).
25 Schintler, L. A., Kulkarni, R., Gorman, S. & Stough, R. Using Raster-Based GIS and Graph Theory to Analyze Complex Networks. *Networks and spatial economics* **7**, 301-313, (2007).
26 Gelagay, H. S. & Minale, A. S. Soil loss estimation using GIS and Remote sensing techniques: A case of Koga watershed, Northwestern Ethiopia. *International Soil and Water Conservation Research* **4**, 126-136, (2016).
27 Wang, Y. Y., Wen, A. B., Guo, J., Shi, Z. L. & Yan, D. C. Spatial distribution, sources and ecological risk assessment of heavy metals in Shenjia River watershed of the Three Gorges Reservoir Area. *Journal of Mountain Science* **14**, 325-335, (2017).
28 Habel, M. *et al.* Using the raster calculator tool to appraise riverbed elevation changes nearby hydrotechnical objects on alluvial rivers. Monitoring 2019. *Published by European Association of Geoscientists & Engineers. https://doi.org/10.3997/2214-4609.201903230* **2019**, 1-5, (2019).
29 Istadi, B. P., Pramono, G. H., Sumintadireja, P. & Alam, S. Modeling study of growth and potential geohazard for LUSI mud volcano: East Java, Indonesia. *Marine and Petroleum Geology* **26**, 1724-1739, (2009).
30 Buchwitz, M. *et al.* Satellite-derived methane hotspot emission estimates using a fast data-driven method. *Atmos Chem Phys* **17**, 5751-5774, (2017).
31 Crippa, M. *et al.* Fossil CO2 and GHG emissions of all world countries: 2019 report. *Report, EUR 29849 EN, Publications Office of the European Union, Luxembourg, 2019, ISBN 978-92-76-11100-9, doi:10.2760/687800, JRC117610*, (2019).
32 van der Werf, G. R. *et al.* Global fire emissions estimates during 1997-2016. *Earth Syst Sci Data* **9**, 697-720, (2017).
33 Bloom, A. A. *et al.* A global wetland methane emissions and uncertainty dataset for atmospheric chemical transport models (WetCHARTs version 1.0). *Geosci. Model Dev.* **10**, 2141-2156, (2017).
34 Hu, H. L. *et al.* The operational methane retrieval algorithm for TROPOMI. *Atmos Meas Tech* **9**, 5423-5440, (2016).
35 Butz, A. *et al.* TROPOMI aboard Sentinel-5 Precursor: Prospective performance of CH4 retrievals for aerosol and cirrus loaded atmospheres. *Remote sensing of environment* **120**, 267-276, (2012).
36 Hasekamp, O. *et al.* Algorithm Theoretical Baseline Document for Sentinel-5 Precursor methane retrieval. *http://www.tropomi.eu/documents/atbd/* **SRON-S5P-LEV2-RP-001**, (2019).

37 Zaputlyaeva, A., Mazzini, A., Caracausi, A. & Sciarra, A. Mantle-Derived Fluids in the East Java Sedimentary Basin, Indonesia. *Journal of Geophysical Research: Solid Earth* **124**, 7962-7977, (2019).